JGR Space Physics

RESEARCH ARTICLE
10.1029/2019JA027569

Special Section:
Early results from the Global-scale Observations of the Limb and Disk (GOLD) mission

Coordinated Ground-Based and Space-Based Observations of Equatorial Plasma Bubbles

Ercha Aa[1,2], Shasha Zou[1], Richard Eastes[3], Deepak K. Karan[3], Shun-Rong Zhang[2], Philip J. Erickson[2], and Anthea J. Coster[2]

[1]Department of Climate and Space Sciences and Engineering, University of Michigan, Ann Arbor, MI, USA, [2]Haystack Observatory, Massachusetts Institute of Technology, Westford, MA, USA, [3]Laboratory for Atmospheric and Space Physics, University of Colorado Boulder, Boulder, CO, USA

Abstract This paper presents coordinated and fortuitous ground-based and spaceborne observations of equatorial plasma bubbles (EPBs) over the South American area on 24 October 2018, combining the following measurements: Global-scale Observations of Limb and Disk far ultraviolet emission images, Global Navigation Satellite System total electron content data, Swarm in situ plasma density observations, ionosonde virtual height and drift data, and cloud brightness temperature data. The new observations from the Global-scale Observations of Limb and Disk/ultraviolet imaging spectrograph taken at geostationary orbit provide a unique opportunity to image the evolution of plasma bubbles near the *F* peak height over a large geographic area from a fixed longitude location. The combined multi-instrument measurements provide a more integrated and comprehensive way to study the morphological structure, development, and seeding mechanism of EPBs. The main results of this study are as follows: (1) The bubbles developed a westward tilted structure with 10–15° inclination relative to the local geomagnetic field lines, with eastward drift velocity of 80–120 m/s near the magnetic equator that gradually decreased with increasing altitude/latitude. (2) Wave-like oscillations in the bottomside *F* layer and detrended total electron content were observed, which are probably due to upward propagating atmospheric gravity waves. The wavelength based on the medium-scale traveling ionospheric disturbance signature was consistent with the interbubble distance of ~500–800 km. (3) The atmospheric gravity waves that originated from tropospheric convective zone are likely to play an important role in seeding the development of this equatorial EPBs event.

Plain Language Summary This study presents multi-instrument observations of equatorial plasma density depletions occurred on 24 October 2018 by using Global-scale Observations of Limb and Disk far ultraviolet images, Global Navigation Satellite System total electron content data, electron density measurements from Swarm satellite, ionosonde measurements, and cloud temperature data. This multi-instrument study generated an integrated and detailed image revealing both large-scale and mesoscale structures of the equatorial plasma depletion. Our results also suggest that atmospheric gravity waves originating from tropospheric convection activity could play a significant seeding role in the development of equatorial plasma bubbles.

Key Points:
- Combined GOLD/UV spectrograph images and ground-based TEC data revealed EPB features and development over a large geographic area
- Bottomside *F* layer oscillations and traveling ionospheric disturbance were observed by ionosonde and detrended TEC results
- Atmospheric gravity waves likely play an important role in seeding the R-T instability and the development of this EPB event

Correspondence to:
E. Aa,
aercha@mit.edu

Citation:
Aa, E., Zou, S., Eastes, R., Karan, D. K., Zhang, S.-R., Erickson, P. J., & Coster, A. J. (2020). Coordinated ground-based and space-based observations of equatorial plasma bubbles. *Journal of Geophysical Research: Space Physics*, *125*. e2019JA027569. https://doi.org/10.1029/2019JA027569

Received 25 OCT 2019
Accepted 12 DEC 2019
Accepted article online 26 DEC 2019

1. Introduction

Equatorial plasma bubbles (EPBs) refer to irregular structures of plasma density depletion that are usually observed in the equatorial and low latitude *F* region during postsunset period. Typical density irregularities within EPBs can have different scale sizes of several to hundreds of kilometers, and EPBs can cover a broad altitudinal range from the bottomside ionosphere up to ~1,000 km (Cherniak et al., 2019; Lühr et al., 2014). One of the top research priorities in the global space weather community is to better understand the generation mechanisms and the dynamic features of EPBs, because they can severely disrupt the amplitude and phase of transionospheric radio waves so as to cause adverse effects on relevant communication and navigation systems. It is generally accepted that EPBs are triggered under a favorable condition of the generalized Rayleigh-Taylor (R-T) instability at the bottomside of the *F* layer, where a steep vertical density gradient forms after the *E* layer disappears postsunset due to high recombination rate. During quiet times, the prereversal enhancement (PRE) of the zonal electric field is responsible for the enhanced upward $\mathbf{E} \times \mathbf{B}$ drift after sunset, which elevates the ionospheric height and subsequently amplifies the growth rate of R-T

instability (Abdu, 2005; Carter et al., 2013; Fejer et al., 1999; Kil, 2015; Woodman & La Hoz, 1976). Thus, initial density perturbations at the bottomside *F* layer can then evolve into EPBs and develop nonlinearly after rising to the topside ionosphere.

The morphological features and spatial/temporal variability of EPBs have been widely investigated via case studies and statistical analysis using different observational methods. For example, the structure of EPBs can be observed from irregular traces of range-type equatorial spread *F* in ionograms (Abdu, 2012; Hysell, 2000; Li et al., 2018; Tsunoda, 2015). The spatial variation of EPBs can be derived from the dark streaks of emission depletion in optical observations from ground-based all-sky imagers (ASIs) or space-based ultraviolet (UV) imaging spectrographs (Comberiate & Paxton, 2010; Hickey et al., 2018; Kelley et al., 2003; Kil et al., 2009; Makela, 2006; Martinis et al., 2015; Otsuka et al., 2002; Shiokawa et al., 2015). In addition, the altitudinal information of irregularities embedded within EPBs can be examined through observations of plume-like structures from coherent backscatter radar or incoherent scatter radar measurements (Ajith et al., 2015; Jin et al., 2018; Li et al., 2013; Rodrigues et al., 2018; Tulasi Ram et al., 2017; Yokoyama & Fukao, 2006). Furthermore, the temporal variation and occurrence distribution of irregularities/bubbles can be extracted from in situ satellite observations, such as the Defense Meteorological Satellite Program constellation (Burke, Gentile, et al., 2004; Burke, Huang, et al., 2004; Huang et al., 2002), Communications/Navigation Outrage Forecasting System (C/NOFS) satellite (Huang et al., 2014; Smith & Heelis, 2017), and Swarm constellation (Xiong et al., 2016; Zakharenkova et al., 2016). Moreover, with the fast-growing and global availability of ground-based Global Navigation Satellite Systems (GNSS) measurements and space-based radio occultation data, the evolution characteristics of EPBs can be monitored continuously on both global or regional scales (Aa et al., 2018; Barros et al., 2018; Buhari et al., 2014, 2017; Cherniak & Zakharenkova, 2016; Cherniak et al., 2014; Katamzi-Joseph et al., 2017; Ma & Maruyama, 2006; Nishioka et al., 2008; Takahashi et al., 2015).

Although EPBs have been extensively studied for several decades, there are still some important and challenging tasks that need to be performed to improve current understanding of their detailed spatial/temporal structures and seeding mechanisms. In this regard, different instruments have their own advantages and limitations in analyzing EPBs: (1) Coherent/incoherent scatter radars can monitor irregularities at high spatial resolution, but their location and field-of-view limit their coverage range. (2) Optical measurements of ASIs are limited with their field of view, and their availability depends on weather conditions. For this reason, multiple ASIs are usually required to get a complete evolution of EPBs structures. (3) Low-Earth orbiting satellite observations can produce in situ density profiles or UV radiance images of irregularities at high spatial resolution, but they can only sample a narrow swath of the EPBs structures along the track of the satellite. (4) Global/regional GNSS total electron content (TEC) observations can monitor ionospheric variability continuously; however, the small-scale structures characteristic of EPBs will sometimes be smoothed out because of the integrating nature of the TEC calculation, not to mention huge data gaps that still exist over receiver-sparse areas, such as oceans.

For these reasons, collective analysis of multisite and multi-instrument measurements provides an effective way to generate an integrated and comprehensive image for specifying both large-scale and mesoscale features of plasma bubbles (Aa et al., 2019; Cherniak et al., 2019). Recently, with the successful launch and deployment of National Aeronautics and Space Administration's Global-scale Observations of Limb and Disk (GOLD) mission, an excellent opportunity exists to use the unique data set from the GOLD far ultraviolet imaging spectrograph to monitor equatorial ionospheric structure. In this paper, we present coordinated ground-based and spaceborne observations of an EPBs event, which occurred on 24 October 2018. Our analysis uses multi-instrument measurements: GOLD/UV imaging spectrograph, TEC from GNSS receiver networks, Swarm in situ density observations, ionosonde measurements, and cloud temperature data. We use these observations to implement a comprehensive analysis of the structural evolution and relevant seeding mechanisms of EPBs.

2. Data Description

The GOLD mission was launched on 25 January 2018 and started its operational observations in October 2018. The main scientific objective of GOLD is to understand the "weather" response of the Earth's thermosphere and ionosphere system to forcing from above and below, and the formation and evolution of EPBs is a primary scientific question (Eastes et al., 2017, 2019). Operating at geostationary orbit over the longitude of 47.5°W, GOLD has an unparalleled advantage of "staring" at the American region from a fixed geographic

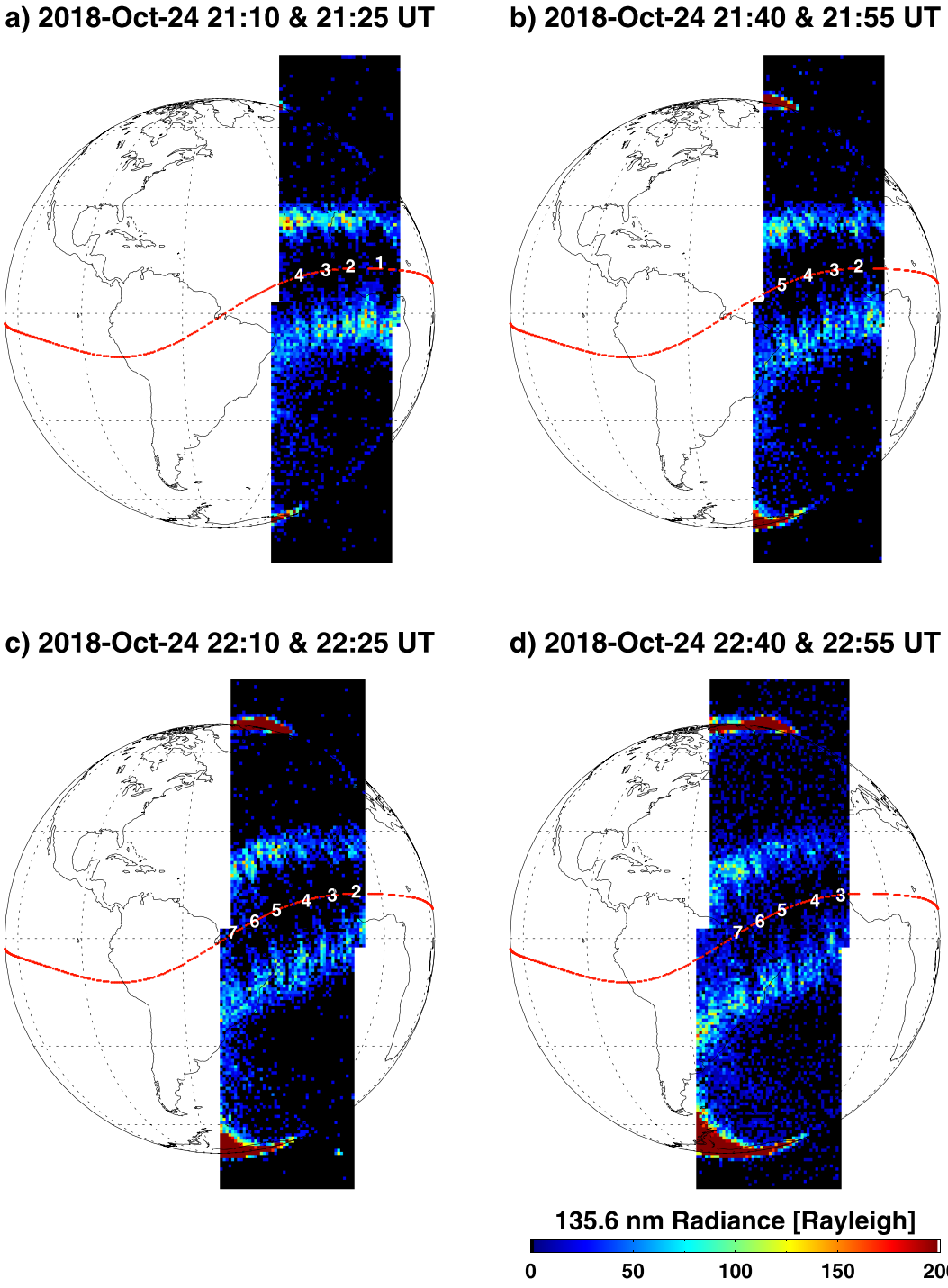

Figure 1. (a–d) OI 135.6-nm radiance maps observed in successive disk scan of GOLD/UV nighttime imaging during 21:10–22:55 UT on 24 October 2018. The dark streaks marked by different numbers represent the optical signature of EPBs. The geomagnetic equator is also shown by red dashed lines. GOLD = Global-scale Observations of the Limb and Disk; UV = ultraviolet; EPBs = equatorial plasma bubbles.

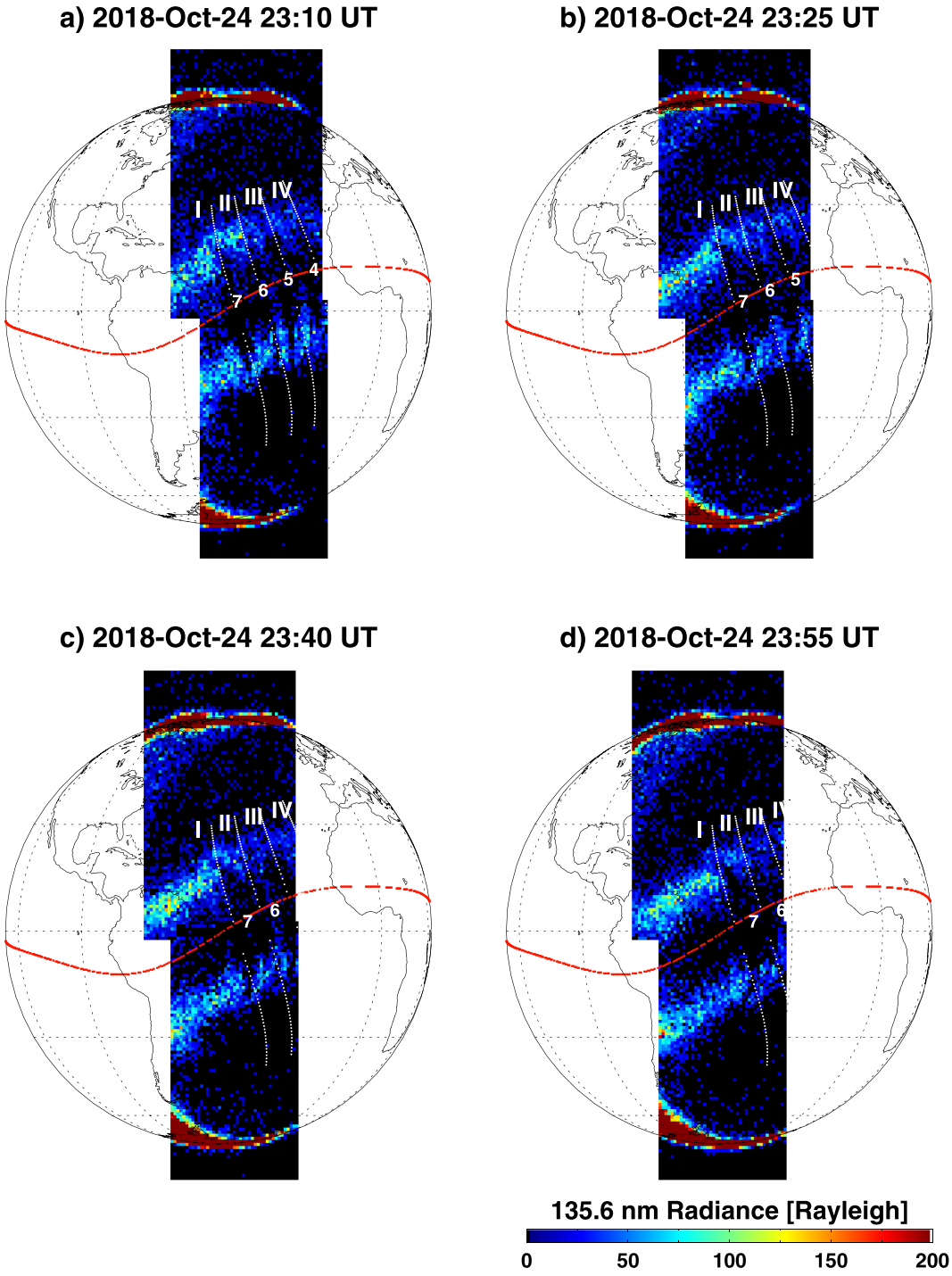

Figure 2. The same as Figure 1 but during the time interval of 23:10–23:55 UT on 24 October 2018. The white dotted curves show four different geomagnetic field lines that go across the EPBs. EPBs = equatorial plasma bubbles.

location for extended periods of time, providing an exact time-evolving map that can unambiguously specify the spatiotemporal variability of Earth's thermosphere and ionosphere system. The GOLD instrument is a far ultraviolet imaging spectrograph that measures Earth's airglow emissions from 132 to 162 nm, which can be used to infer thermospheric temperature and composition on the dayside disk as well as equatorial ionospheric structures on the nightside. The nighttime disk images of atomic oxygen 135.6-nm emissions, which have a spatial resolution ~100 km in the longitudinal direction and ~50 km in the latitudinal direction, will be used in this study to derive valuable information on the low latitude ionosphere.

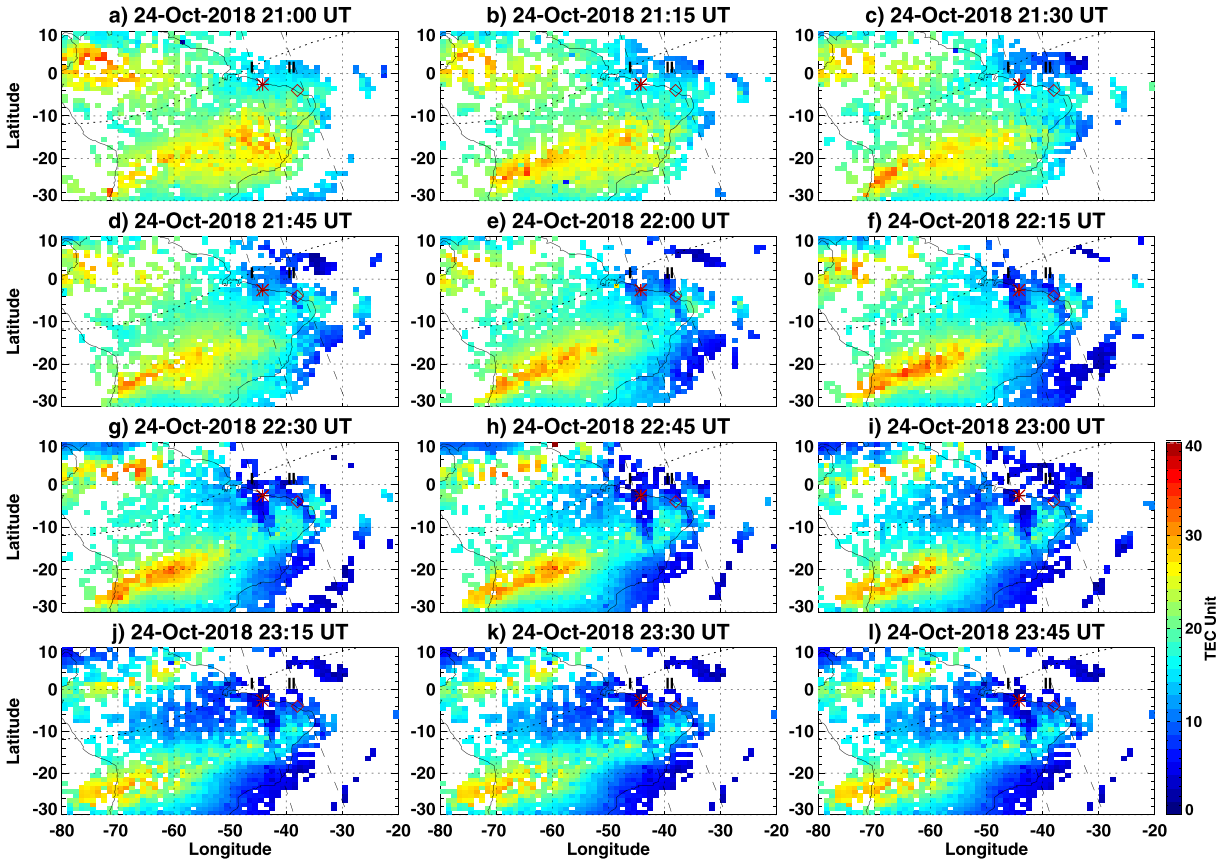

Figure 3. (a–l) Gridded TEC maps over South American regions with 15-min interval during 21:00–23:45 UT on 24 October 2018. The ionosonde stations of Sao Luis and Fortaleza are marked with asterisk and diamond, respectively. Two geomagnetic field lines ("I" and "II") that go across the EPBs are marked in dashed lines, and the geomagnetic equator is shown in dotted line. EPBs = equatorial plasma bubbles.

Gridded TEC products from the Madrigal distributed data system are also used to study EPBs structures. TEC data are produced and provided through the Madrigal distributed data system developed at the Massachusetts Institute of Technology's Haystack Observatory by using dense networks of worldwide GNSS receivers and have a resolution of 1° (latitude) × 1° (longitude) × 5 min (Rideout & Coster, 2006; Vierinen et al., 2016). Moreover, ionosonde measurements from Sao Luis (2.6°S, 315.8°E) and Fortaleza (3.9°S, 321.6°E), as well as in situ plasma density measurements onboard the Swarm A/C satellites, are also used here to analyze the characteristics of plasma irregularities.

Localized gravity waves that originated from the tropospheric convective zone could be an essential factor in seeding EPBs, and the deep convection activity can be deduced from cloud temperature data. These data are derived from global (60°S to 60°N) 4-km pixel-resolution infrared brightness temperature data, merged from selected geostationary satellites measurements over the period of record (i.e., Geosynchronous Operational Environmental Satellites [GOES]-8/9/10/11/12/13/14/15/16, United States; the Meteorological Satellite [Meteosat]-5/7/8/9/10, European Community; Geosynchronous Meteorological Satellite[GMS]-5/Multifunctional Transport Satellite[MTSat]-1R/2/Himawari-8, Japan) (Janowiak et al., 2017).

3. Results

EPBs are known to produce optical signatures observed as streaks of reduced emission in spaceborne UV imaging spectrographs (Kelley et al., 2003; Kil et al., 2004). Figure 1 shows continuous OI 135.6-nm radiance maps observed by GOLD in successive disk scans during 21:10–22:55 UT on 24 October 2018. The bright zonal band in the low-latitude region paralleling the magnetic equator (red line) is produced by enhanced oxygen ion density in the equatorial ionization anomaly (EIA) region. The dark streaks that cut through

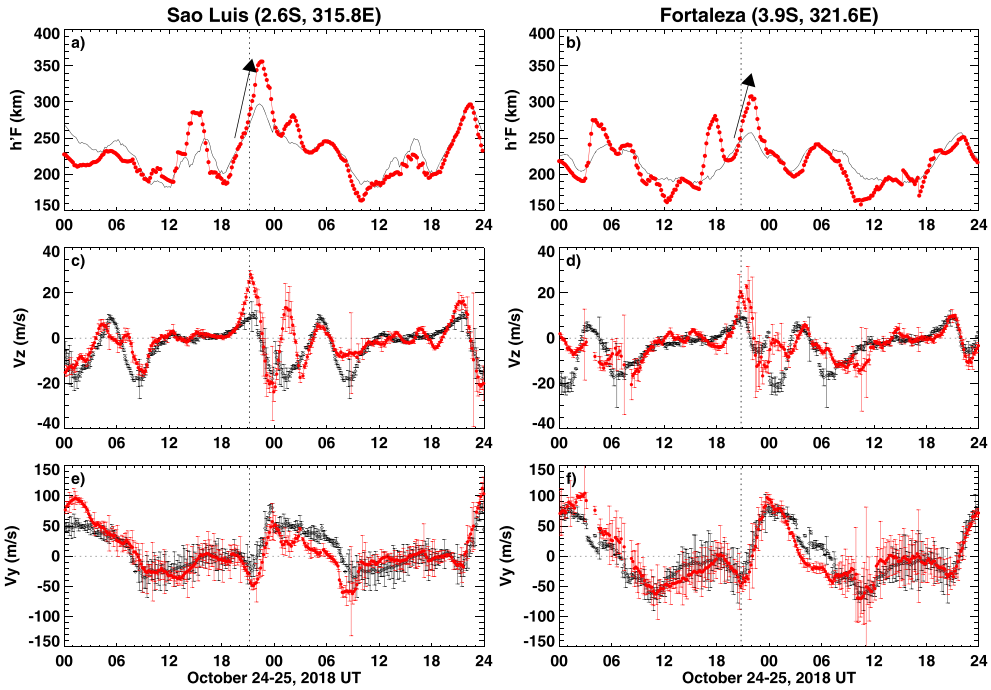

Figure 4. The temporal variation of ionospheric h'F, *F* layer vertical drift, and zonal drift velocity observed at Sao Luis (a, c, and e) and Fortaleza (b, d, and f) during the period of 24–25 October 2018. The black lines represent the values of previous 5-day average. The vertical dotted line represents the local sunset. The error bars represent the velocity spread.

the EIA band represent reduced emissions caused by low density within plasma bubbles. There are seven discernible dark streaks marked with #1–7 from east to west. These streaks elongate from northwest to southeast direction, with a meridional length of ~1,500–2,000 km and interbubble distance of ~500–800 km. Moreover, Figure 2 displays similar UV images for later time periods of 23:10–23:55 UT on 24 October 2018. The white dotted curves show four different geomagnetic field lines (marked with I, II, III, and IV) along which the EPBs were approximately extending. When comparing the consecutive images, the EPBs depletion streaks were found to be drifting eastward and developing westward tilted (or backward C-shape) structure. The tilt angle ranges from 10–15° relative to the Earth's magnetic field line (Figures 2c and 2d). The airglow signature of EPBs and the tilted structure were also illustrated in simulations (Retterer, 2010) and are consistent with the previous ground-based and spaceborne observations (Jin et al., 2018; Kelley et al., 2003; Kil et al., 2009; Li et al., 2018; Tsunoda et al., 1982), which will be further discussed in the next section.

Besides the UV images, the EPBs can also be observed in two-dimensional TEC maps as a depletion structure perpendicular to the geomagnetic equator. Figure 3 shows 12 successive TEC maps over the South American region with 15-min cadence during 21:00–23:45 UT on 24 October 2018. The EIA crests can be seen as two regions with enhanced TEC about 10° north and south of the geomagnetic equator (black dotted line). Two TEC depletion belts are parallel to the magnetic field lines, as highlighted by the black dashed lines, which exist over the equatorial region around 45°W and 40°W. Comparing with the surrounding region, the amplitude of the TEC depletion within these EPBs is approximately 10 TEC unit (10^{16} el/m^2). Taking the left-side branch of the depletion as an example, we find an onset time of around 22 UT with a subsequent gradual extension toward the EIA crest along the geomagnetic field line "I," which is the same field line as that marked in Figure 2. The EPB along field line "II" also exhibited similar but weaker evolution.

Moreover, there are two ionosondes, that is, Sao Luis and Fortaleza, which are located near these two depletion belts and are labeled as asterisk and diamond in Figure 3. Figure 4 shows the *F* layer bottomside virtual height (h'F), vertical drift velocity, and zonal drift velocity measured by these two ionosondes on 24 October 2018 (red), as compared with the previous 5-day averaged values (black). It can be seen from the top panels that the h'F over Sao Luis exhibited a significant PREs (marked with an arrow) from 250 to 360 km at around 21 UT on 24 October, while the 5-day averaged peak value of PREs is less than 300 km. A considerable h'F elevation around the same time can be also observed for Fortaleza station, with the peak value

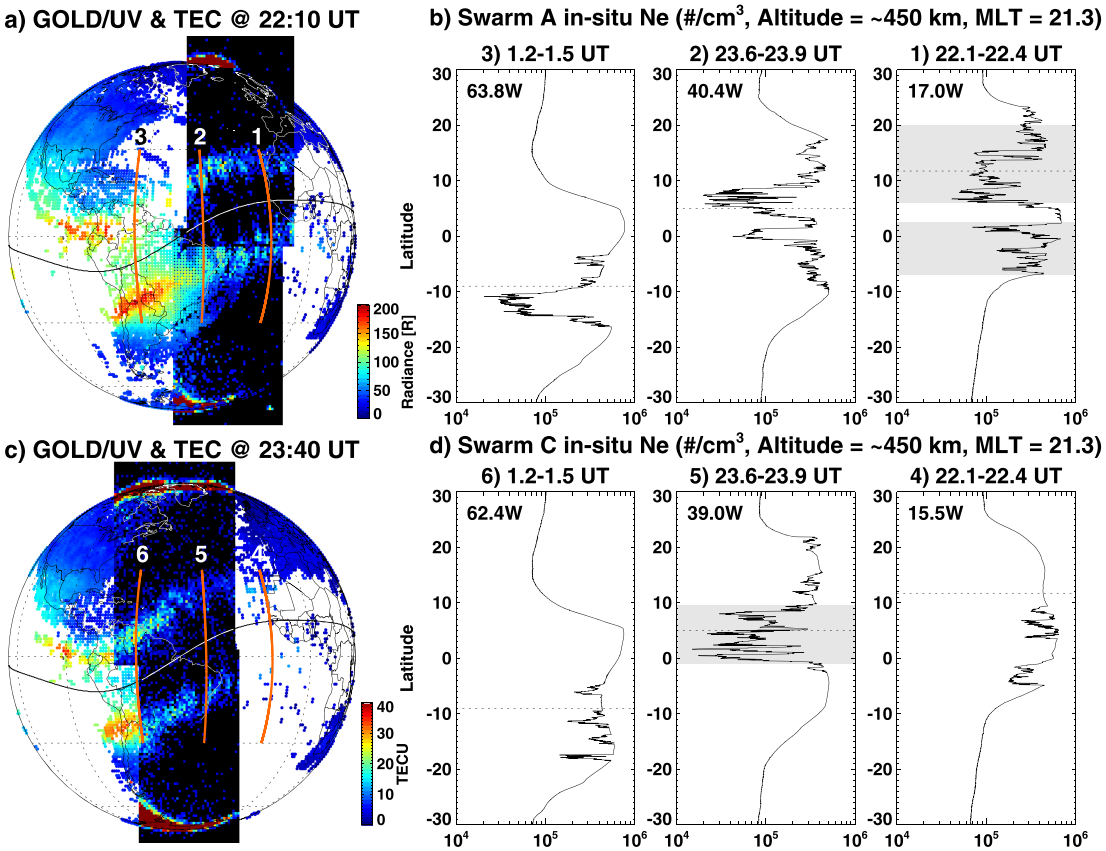

Figure 5. (a) Combined global map of GNSS TEC and OI 135.6-nm radiance of GOLD/UV imaging at 22:10 UT with three consecutive satellite paths of Swarm A. (b) Variation of in situ electron density as a function of latitudes along these paths. (c, d) The same as Figures 5a and 5b, respectively, but at 23:40 UT and for Swarm C satellite paths. The shaded areas represent certain plasma depletions. The magnetic equator is marked by solid line in left panels and dotted line in right panels. GNSS = Global Navigation Satellite System; TEC = total electron content; GOLD = Global-scale Observations of the Limb and Disk; UV = ultraviolet.

of PREs (310 km) on 24 October larger than 5-day average one (250 km). The corresponding peak velocity of vertical drift shown in Figures 4c and 4d, which is 30 m/s over Sao Luis and 25 m/s over Fortaleza, also displayed considerable increase compared with the 5-day averaged values (~10 m/s). These collectively demonstrate the presence of an enhanced dusk sector zonal electric field, raising the *F* layer and amplifying the growth rate of the R-T instability to generate the observed EPBs. The zonal drift exhibited eastward velocity after the PREs.

The nighttime GOLD/UV OI 135.6-nm images were mainly fixed at the American-Atlantic longitudes. The TEC maps have a broader coverage but with data gaps over the ocean, especially near the Northern Hemisphere part of the EIA. These two data sets complement each other and thus were combined to generate a map shown in Figure 5, which provides a much broader spatial context for EPBs. The extension of EPBs to the southern EIA crest and the backward C-shape streak spanning both hemispheres are clearly indicated. Furthermore, three consecutive satellite passes of Swarm A/C and the corresponding latitudinal profiles of the in situ electron density along these orbits are also shown in Figure 5. Both Swarm A and Swarm C flew at the height of ~450 km and were located at nearby longitudes around 09 LT (dayside) and 21 LT (nightside). Swarm B is not shown here since it did not pass through the American sector at local dusk hours during this period. The signature of plasma irregularities can be clearly seen in Orbit #1 (17.0°W) of Swarm A during 22:00–22:30 UT and Orbit #5 (39.0°W) of Swarm C during 23:30–00:00 UT, where considerable plasma density bite outs with sawtooth-like irregular fluctuations were measured near the magnetic equator (horizontal dotted line). This revealed the presence of small-scale density fluctuations within the EPBs seen in the GOLD/UV imaging and GNSS TEC results. Although Swarm A and C were very close to each other and passed the EPBs nearly the same time, there are certain spatial differences in the small-scale structures that are observed by them (e.g., compare panels 1 and 4).

4. Discussion

First, the development of the westward tilt (or backward C-shape) of the EPBs depletion has been clearly shown in GOLD/UV optical images in Figures 1 and 2. This shape has previously been suggested to be caused by latitudinal variation of zonal plasma drift and/or the polarization electric field inside the EPBs. As described in the principle of *F* region dynamo theory (Rishbeth, 1997): The neutral wind in the postsunset sector is typically eastward at low latitudes, which generates a downward *F* region dynamo electric field. This vertical electric field further drives an eastward $E \times B$ drift of the *F* region plasma with nearly similar velocities as the neutral wind. During this study event, estimation of the eastward drift velocity of 80–120 m/s near the magnetic equator can be achieved through comparing the differences (~2–3°) of the central location of the Dark Streaks #1 between Figures 2a and 2d, which is consistent with the zonal drift velocities measured by ionosondes in Figures 4e and 4f and previous experimental/modeling studies of EPBs zonal drift velocities (Chapagain et al., 2012; Gurav et al., 2018; Huba et al., 2009; Sun et al., 2016). Furthermore, both numerical calculations and in situ observations have previously shown that this zonal plasma eastward drift often decreases with increasing altitude/latitude and thus forming a backward C-shape (Kil et al., 2002; Martinis et al., 2003; Pimenta et al., 2003). On the other hand, Kil et al. (2009) and Huang et al. (2010) suggested that a polarization electric field can develop inside the plasma depletion region due to conductivity gradients, which can also retard the eastward flow of the plasma depletion structures.

Second, in addition to generally favorable condition for the R-T instability created by the usual PRE, various mechanisms have been proposed as possible seeding factors that can trigger initial plasma density perturbations on the bottom side *F* layer. These include (1) enhanced zonal eastward electric field due to solar wind-magnetosphere-ionosphere coupling processes. The prompt penetration electric field from high latitude to low latitude can increase the *F* layer vertical drift on the daytime through dusk sectors and thus facilitate the development of EPBs (Abdu et al., 2003; Basu et al., 2007; Ebihara & Tanaka, 2015; Tulasi Ram et al., 2008). (2) Gravity waves from the lower atmosphere. Gravity waves generated by upward propagating meteorological processes in the lower atmosphere may modulate the bottomside *F* layer plasma, producing large-scale wave structures with periodic spacing, which may accelerate the *F* layer uplifting and trigger EPBs (Abdu et al., 2009; McClure et al., 1998; Retterer & Roddy, 2014; Tsunoda, 2010; Tsunoda et al., 2011; Tulasi Ram et al., 2014). (3) Neutral wind shear. Some studies suggested that vertical shear in the zonal winds could cause wave-like vortex, which has a rapid growth rate that can seed the R-T instability and initiate plasma irregularities (Hysell et al., 2005, 2006; Kudeki et al., 2007). (4) Nighttime medium-scale traveling ionospheric disturbances (MSTIDs) due to Perkins/Es instabilities (Perkins, 1973). The polarization electric field within MSTIDs can map along the geomagnetic field lines to the equatorial bottomside *F* layer to initiate the EPBs (Krall et al., 2011; Miller et al., 2009; Taori et al., 2015; Valladares & Sheehan, 2016).

For the current EPBs case, the geomagnetic activity condition was relatively quiet on 24 October 2018 with the interplanetary magnetic field Bz close to 0 and no geomagnetic storm or substorm onset within a few hours before the observed EPBs (Figure 6a). The possibility of significant external driving forces (e.g., interplanetary electric fields) from the magnetosphere for EPBs in the postsunset sector is unlikely under this circumstance. Figure 6b displays the rate of TEC index (ROTI) map to illustrate the ionospheric irregularities between 35°W and 55°W over the South American sector. Next, we discuss the possibility of forcing from below. Figure 6c shows the temporal variation of the electron density profile at Sao Luis between 12 and 24 UT on 24 October 2018. Of particular note, the ionosonde-retrieved topside profile above the *F*2 peak is obtained assuming a α-Chapman shape of plasma distribution (Reinisch & Huang, 2001), and thus, only the bottomside profile should be examined. Three continuous quasiperiodic (~50 min) wave-like modulations of the bottomside *F* layer height marked by white arrows can be clearly seen between 22 and 24 UT. Moreover, Figure 6d shows the *F* layer true height as observed by the Digisonde at specific plasma frequencies (3.0–6.5 MHz) over Sao Luis, plotted from 18 to 24 UT. There was a clear downward phase propagation (marked with a dashed line), which identifies the possible presence of atmospheric gravity waves (AGWs) (Abdu et al., 2009; Mandal et al., 2019). Furthermore, Figure 6e shows a keogram plot of detrended TEC as a function of latitude and time at 48°W longitude that around the EPBs region. Detrended TEC was calculated using the same method mentioned in Coster et al. (2017) and Zhang et al. (2017), where 1-hr TEC moving average was subtracted. MSTIDs that represent the ionospheric signature of AGWs are clearly observed in detrended TEC. Several possible traveling ionospheric disturbance (TID) wavefronts (marked with dashed lines) can also be clearly seen with an estimated propagation velocity of ~200–300 m/s and wavelength of ~500–800 km. The latter is close to the value of interbubble distance shown in GOLD/UV and TEC images.

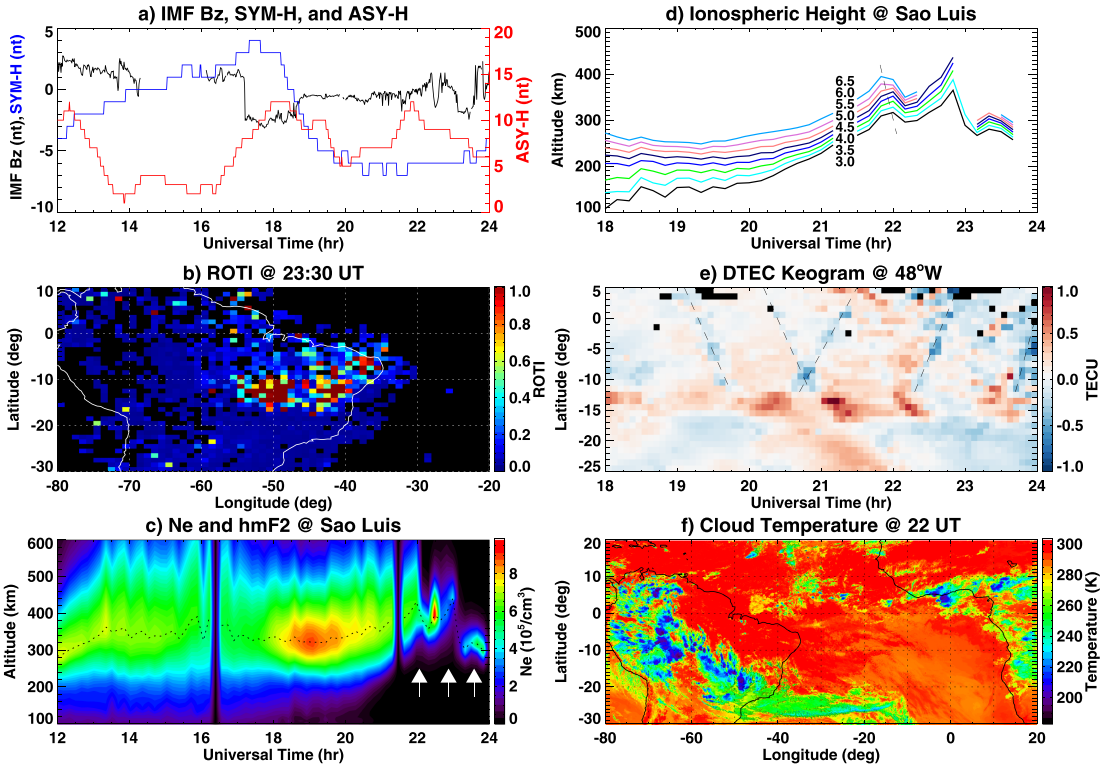

Figure 6. (a) Temporal variation of interplanetary magnetic field (IMF) Bz, the longitudinal asymmetric index (ASY-H), and the symmetric index (SYM-H) between 12 and 24 UT. (b) Rate of TEC index plot at 23:30 UT. (c) Electron density profile and *hmF*2 at Sao Luis between 12 and 24 UT. Three quasiperiodic wave-like structures are marked by arrows. (d) Variation of *F* layer true heights for different frequencies (3.0–6.5 MHz) at Sao Luis. (e) Keogram plot of detrended total electron content (TEC) as a function of latitude and time at 48°W longitude between 18 and 24 UT. The TID structures are marked by dashed lines. (f) Observation of deep clouds in brightness temperature at 22 UT. All six images are for 24 October 2018.

Many studies have demonstrated that such AGWs can be generated in the tropospheric convective region near the intertropical convergence zone and can grow exponentially when propagating all the way upward into the thermosphere-ionosphere system before being entirely dissipated (Li et al., 2016; Vadas, 2007; Yiğit et al., 2012; Yizengaw & Groves, 2018). However, considering that troposphere excitation sources can be highly mobile and that wave propagation along the long path is strongly influenced by low atmosphere variability, the manifestation of TIDs in the keogram might not be so regular and well organized. Thus, in order to further specify the potential source of the AGW/TIDs, Figure 6f shows an observation of deep clouds in brightness temperature at 22 UT on 24 October 2018. The purple to blue areas in South American and West African areas indicate that temperature was lower than 210 K, a signature suggesting that the tops of thunderstorms protrude well into the tropopause region (Hoffmann & Alexander, 2010). Such objects are referred to as deep convective clouds and can be an important source for the generation of upward propagating AGWs (Azeem et al., 2015; Jonah et al., 2018; Vadas & Liu, 2009). In particular, these studies indicated that concentric secondary gravity waves and TIDs with a wavelength of several hundreds to thousands of kilometers can be triggered by troposphere convection and detected at ionospheric heights. The deep convection activity shown here occurred in the local afternoon and continued for several hours, which was during the similar periods and in locations adjacent to where the MSTIDs were observed. Therefore, the combination of these mutually supportive pieces of evidence collectively suggests that convectively induced AGW/TIDs could have seeded the EPBs in this current case.

5. Conclusion

This paper presents coordinated ground-based and spaceborne observational analysis of EPBs over the South American area on 24 October 2018. The morphological structure and seeding mechanism of the bubbles were analyzed by using multi-instrument measurements, including the GOLD/UV imaging spectrograph, GNSS TEC maps, Swarm in situ electron density data, ionosonde measurements, and cloud temperature

data. The new observations provided by GOLD/UV geosynchronous images provide a unique tool for studies of plasma irregularity evolution and equatorial ionospheric dynamics from a fixed longitude location. Furthermore, a combination of different measurements provides a powerful tool for the space weather community to achieve a more integrated and detailed view on plasma irregularity structure. The main results can be summarized as follows: (1) The plasma depletion developed westward tilted structure of 10–15° relative to the Earth's magnetic field line, with an eastward drift velocity of 80–120 m/s near the magnetic equator that gradually decreased with increasing altitude/latitude. (2) Wave-like oscillations of traveling ionospheric disturbances were observed both in ionosonde electron density profiles and detrended TEC keograms. Observed wavelengths were consistent with interbubble distances of 500–800 km. (3) Atmospheric gravity waves originating from the tropospheric convective zone are suggested to be a possible seeding process for the development of this EPBs event.

Acknowledgments
We greatly appreciate NASA/GOLD mission science team for providing data to the public (gold.cs.ucf.edu). We acknowledge ESA for providing the SWARM data (http://earth.esa.int/swarm). GPS TEC data products and access through the Madrigal distributed data system are provided to the community (http://cedar.openmadrigal.org/) by the Massachusetts Institute of Technology (MIT) under support from U.S. National Science Foundation Grant AGS-1762141. S. Zou acknowledges NASA80NSSC20K0190 for the support of this work. A. J. C. and S. R. Z. acknowledge the ONR Grant N00014-17-1-2186, and S. R. Z. and A. J. C. acknowledge the AFOSR MURI Grant FA9559-16-1-0364. Data for the TEC processing are provided from the following organizations: The Crustal Dynamics Data Information System (CDDIS), the Scripps Orbit and Permanent Array Center (SOPAC), the Continuously Operating Reference System (CORS), the EUREF Permanent GNSS network (EPN), the University NAVSTAR Consortium (UNAVCO), Institut Geographique National in France (IGN), the Brazilian Network for Continuous Monitoring (RBMC), National Geodetic Survey, Instituto Brasileiro de Geografia e Estatística, RAMSAC CORS of Instituto Geográfico Nacional de la República Argentina, Arecibo Observatory, Low-Latitude Ionospheric Sensor Network (LISN), Topcon Positioning Systems, Inc., Canadian High Arctic Ionospheric Network, Centro di Ricerche Sismologiche, Système d'Observation du Niveau des Eaux Littorales (SONEL), RENAG : REseau NAtional GPS permanent, GeoNet - the official source of geological hazard information for New Zealand, GNSS Reference Networks, Finnish Meteorological Institute, and SWEPOS-Sweden. The IMF, ASY-H, and SYM-H data are obtained from NASA/GSFCs Space Physics Data Facilitys OMNIWeb service (https://cdaweb.gsfc.nasa.gov/). We acknowledge the University of Massachusetts Lowell for providing ionosonde data from the DIDB database of Global Ionospheric Radio Observatory (http://giro.uml.edu/). The cloud brightness temperature (BT) data were provided by the National Aeronautics and Space Administration (NASA) Goddard Earth Sciences Data and Information Services Central (https://disc.gsfc.nasa.gov/).

References

Aa, E., Huang, W., Liu, S., Ridley, A., Zou, S., Shi, L., et al. (2018). Midlatitude plasma bubbles over China and adjacent areas during a magnetic storm on 8 September 2017. *Space Weather*, *16*, 321–331. https://doi.org/10.1002/2017SW001776

Aa, E., Zou, S., Ridley, A. J., Zhang, S.-R., Coster, A. J., Erickson, P. J., et al. (2019). Merging of storm-time midlatitude traveling ionospheric disturbances and equatorial plasma bubbles. *Space Weather*, *17*, 285–298. https://doi.org/10.1029/2018SW002101

Abdu, M. A. (2005). Equatorial ionosphere thermosphere system: Electrodynamics and irregularities. *Advances in Space Research*, *35*, 771–787. https://doi.org/10.1016/j.asr.2005.03.150

Abdu, M. A. (2012). Equatorial spread *F*/plasma bubble irregularities under storm time disturbance electric fields. *Journal of Atmospheric and Terrestrial Physics*, *75*, 44–56. https://doi.org/10.1016/j.jastp.2011.04.024

Abdu, M. A., Alam Kherani, E., Batista, I. S., de Paula, E. R., Fritts, D. C., & Sobral, J. H. A. (2009). Gravity wave initiation of equatorial spread F/plasma bubble irregularities based on observational data from the SpreadFEx campaign. *Annales Geophysicae*, *27*, 2607–2622. https://doi.org/10.5194/angeo-27-2607-2009

Abdu, M. A., Batista, I. S., Takahashi, H., MacDougall, J., Sobral, J. H., Medeiros, A. F., & Trivedi, N. B. (2003). Magnetospheric disturbance induced equatorial plasma bubble development and dynamics: A case study in Brazilian sector. *Journal of Geophysical Research*, *108*(A12), 1449. https://doi.org/10.1029/2002JA009721

Ajith, K. K., Ram, S. T., Yamamoto, M., Yokoyama, T., Gowtam, V. S., Otsuka, Y., et al. (2015). Explicit characteristics of evolutionary-type plasma bubbles observed from Equatorial Atmosphere Radar during the low to moderate solar activity years 2010-2012. *Journal of Geophysical Research: Space Physics*, *120*, 1371–1382. https://doi.org/10.1002/2014JA020878

Azeem, I., Yue, J., Hoffmann, L., Miller, S. D., Straka, W. C., & Crowley, G. (2015). Multisensor profiling of a concentric gravity wave event propagating from the troposphere to the ionosphere. *Geophysical Research Letters*, *42*, 7874–7880. https://doi.org/10.1002/2015GL065903

Barros, D., Takahashi, H., Wrasse, C. M., & Figueiredo, C. A. O. B. (2018). Characteristics of equatorial plasma bubbles observed by TEC map based on ground-based GNSS receivers over South America. *Annales Geophysicae*, *36*, 91–100. https://doi.org/10.5194/angeo-36-91-2018

Basu, S., Basu, S., Rich, F. J., Groves, K. M., MacKenzie, E., Coker, C., et al. (2007). Response of the equatorial ionosphere at dusk to penetration electric fields during intense magnetic storms. *Journal of Geophysical Research*, *112*, A08308. https://doi.org/10.1029/2006JA012192

Buhari, S. M., Abdullah, M., Hasbi, A. M., Otsuka, Y., Yokoyama, T., Nishioka, M., & Tsugawa, T. (2014). Continuous generation and two-dimensional structure of equatorial plasma bubbles observed by high-density GPS receivers in Southeast Asia. *Journal of Geophysical Research: Space Physics*, *119*, 10,569–10,580. https://doi.org/10.1002/2014JA020433

Buhari, S. M., Abdullah, M., Yokoyama, T., Otsuka, Y., Nishioka, M., Hasbi, A. M., et al. (2017). Climatology of successive equatorial plasma bubbles observed by GPS ROTI over Malaysia. *Journal of Geophysical Research: Space Physics*, *122*, 2174–2184. https://doi.org/10.1002/2016JA023202

Burke, W., Gentile, L. C., Huang, C. Y., Valladares, C. E., & Su, S. Y. (2004). Longitudinal variability of equatorial plasma bubbles observed by DMSP and ROCSAT-1. *Journal of Geophysical Research*, *109*, A12301. https://doi.org/10.1029/2004JA010583

Burke, W., Huang, C., Gentile, L., & Bauer, L. (2004). Seasonal-longitudinal variability of equatorial plasma bubbles. *Annales Geophysicae*, *22*, 3089–3098. https://doi.org/10.5194/angeo-22-3089-2004

Carter, B. A., Zhang, K., Norman, R., Kumar, V. V., & Kumar, S. (2013). On the occurrence of equatorial F-region irregularities during solar minimum using radio occultation measurements. *Journal of Geophysical Research: Space Physics*, *118*, 892–904. https://doi.org/10.1002/jgra.50089

Chapagain, N. P., Makela, J. J., Meriwether, J. W., Fisher, D. J., Buriti, R. A., & Medeiros, A. F. (2012). Comparison of nighttime zonal neutral winds and equatorial plasma bubble drift velocities over Brazil. *Journal of Geophysical Research*, *117*, A06309. https://doi.org/10.1029/2012JA017620

Cherniak, I., Krankowski, A., & Zakharenkova, I. (2014). Observation of the ionospheric irregularities over the Northern Hemisphere: Methodology and service. *Radio Science*, *49*, 653–662. https://doi.org/10.1002/2014RS005433

Cherniak, I., & Zakharenkova, I. (2016). First observations of super plasma bubbles in Europe. *Geophysical Research Letters*, *43*, 11,137–11,145. https://doi.org/10.1002/2016GL071421

Cherniak, I., Zakharenkova, I., & Sokolovsky, S. (2019). Multi-instrumental observation of storm-induced ionospheric plasma bubbles at equatorial and middle latitudes. *Journal of Geophysical Research: Space Physics*, *124*, 1491–1508. https://doi.org/10.1029/2018JA026309

Comberiate, J., & Paxton, L. J. (2010). Coordinated UV imaging of equatorial plasma bubbles using TIMED/GUVI and DMSP/SSUSI. *Space Weather*, *8*, S10002. https://doi.org/10.1029/2009SW000546

Coster, A. J., Goncharenko, L., Zhang, S.-R., Erickson, P. J., Rideout, W., & Vierinen, J. (2017). GNSS observations of ionospheric variations during the 21 August 2017 solar eclipse. *Geophysical Research Letters*, *44*, 12,041–12,048. https://doi.org/10.1002/2017GL075774

Eastes, R. W., McClintock, W. E., Burns, A. G., Anderson, D. N., Andersson, L., Codrescu, M., et al. (2017). The global-scale observations of the limb and disk (GOLD) Mission. *Space Science Reviews*, *212*, 383–408. https://doi.org/10.1007/s11214-017-0392-2

Eastes, R. W., Solomon, S. C., Daniell, R. E., Anderson, D. N., Burns, A. G., England, S. L., et al. (2019). Global-scale observations of the equatorial ionization anomaly. *Geophysical Research Letters*, *46*, 9318–9326. https://doi.org/10.1029/2019GL084199

Ebihara, Y., & Tanaka, T. (2015). Substorm simulation: Insight into the mechanisms of initial brightening. *Journal of Geophysical Research: Space Physics*, *120*, 7270–7288. https://doi.org/10.1002/2015JA021516

Fejer, B. G., Scherliess, L., & de Paula, E. R. (1999). Effects of the vertical plasma drift velocity on the generation and evolution of equatorial spread F. *Journal of Geophysical Research*, *104*, 19,859–19,870. https://doi.org/10.1029/1999JA900271

Gurav, O. B., Sharma, A. K., Ghodpage, R. N., Nade, D. P., Chavan, G. A., Gaikwad, H. P., & Patil, P. T. (2018). Zonal drift velocity of equatorial plasma bubbles during ascending phase of 24th solar cycle using all-sky imager over Kolhapur India. *Journal of Geophysical Research: Space Physics*, *123*, 10,266–10,282. https://doi.org/10.1029/2018JA025810

Hickey, D. A., Martinis, C. R., Mendillo, M., Baumgardner, J., Wroten, J., & Milla, M. (2018). Simultaneous 6300 Å airglow and radar observations of ionospheric irregularities and dynamics at the geomagnetic equator. *Annales Geophysicae*, *36*(2), 473–487. https://doi.org/10.5194/angeo-36-473-2018

Hoffmann, L., & Alexander, M. J. (2010). Occurrence frequency of convective gravity waves during the North American thunderstorm season. *Journal of Geophysical Research*, *115*, D20111. https://doi.org/10.1029/2010JD014401

Huang, C.-S., de La Beaujardiere, O., Pfaff, R. F., Retterer, J. M., Roddy, P. A., Hunton, D. E., et al. (2010). Zonal drift of plasma particles inside equatorial plasma bubbles and its relation to the zonal drift of the bubble structure. *Journal of Geophysical Research*, *115*, A07316. https://doi.org/10.1029/2010JA015324

Huang, C.-S., La Beaujardiere, O., Roddy, P. A., Hunton, D. E., Liu, J. Y., & Chen, S. P. (2014). Occurrence probability and amplitude of equatorial ionospheric irregularities associated with plasma bubbles during low and moderate solar activities (2008-2012). *Journal of Geophysical Research: Space Physics*, *119*, 1186–1199. https://doi.org/10.1002/2013JA019212

Huang, C. Y., Burke, W. J., Machuzak, J. S., Gentile, L. C., & Sultan, P. J. (2002). Equatorial plasma bubbles observed by DMSP satellites during a full solar cycle: Toward a global climatology. *Journal of Geophysical Research*, *107*(A12), 1434. https://doi.org/10.1029/2002JA009452

Huba, J. D., Ossakow, S. L., Joyce, G., Krall, J., & England, S. L. (2009). Three-dimensional equatorial spread *F* modeling: Zonal neutral wind effects. *Geophysical Research Letters*, *36*, L19106. https://doi.org/10.1029/2009GL040284

Hysell, D. L. (2000). An overview and synthesis of plasma irregularities in equatorial spread/*F*. *Journal of Atmospheric and Solar-Terrestrial Physics*, *62*, 1037–1056. https://doi.org/10.1016/S1364-6826(00)00095-X

Hysell, D. L., Kudeki, E., & Chau, J. L. (2005). Possible ionospheric preconditioning by shear flow leading to equatorial spread *F*. *Annales Geophysicae*, *23*, 2647–2655. https://doi.org/10.5194/angeo-23-2647-2005

Hysell, D. L., Larsen, M. F., Swenson, C. M., & Wheeler, T. F. (2006). Shear flow effects at the onset of equatorial spread *F*. *Journal of Geophysical Research*, *111*, A11317. https://doi.org/10.1029/2006JA011963

Janowiak, J., Joyce, B., & Xie, P. (2017). NCEP/CPC l3 half hourly 4km global (60°S–60°N) merged IR v1, doi: 10.5067/P4HZB9N27EKU.

Jin, H., Zou, S., Chen, G., Yan, C., Zhang, S., & Yang, G. (2018). Formation and evolution of low-latitude *F* region field-aligned irregularities during the 7–8 September 2017 storm: Hainan coherent scatter phased array radar and Digisonde Observations. *Space Weather*, *16*, 648–659. https://doi.org/10.1029/2018SW001865

Jonah, O. F., Coster, A., Zhang, S., Goncharenko, L., Erickson, P. J., de Paula, E. R., & Kherani, E. A. (2018). TID observations and source analysis during the 2017 Memorial Day weekend geomagnetic storm over North America. *Journal of Geophysical Research: Space Physics*, *123*, 8749–8765. https://doi.org/10.1029/2018JA025367

Katamzi-Joseph, Z. T., Habarulema, J. B., & Hernández-Pajares, M. (2017). Midlatitude postsunset plasma bubbles observed over Europe during intense storms in April 2000 and 2001. *Space Weather*, *15*(9), 1177–1190. https://doi.org/10.1002/2017SW001674

Kelley, M. C., Makela, J. J., Paxton, L. J., Kamalabadi, F., Comberiate, J. M., & Kil, H. (2003). The first coordinated ground- and space-based optical observations of equatorial plasma bubbles. *Geophysical Research Letters*, *30*(14), 1766. https://doi.org/10.1029/2003GL017301

Kil, H. (2015). The morphology of equatorial plasma bubbles—A review. *Journal of Astronomy and Space Sciences*, *32*, 13–19. https://doi.org/10.5140/JASS.2015.32.1.13

Kil, H., Heelis, R. A., Paxton, L. J., & Oh, S.-J. (2009). Formation of a plasma depletion shell in the equatorial ionosphere. *Journal of Geophysical Research*, *114*, A11302. https://doi.org/10.1029/2009JA014369

Kil, H., Kintner, P. M., de Paula, E. R., & Kantor, I. J. (2002). Latitudinal variations of scintillation activity and zonal plasma drifts in South America. *Radio Science*, *37*(1), 1006. https://doi.org/10.1029/2001RS002468

Kil, H., Su, S.-Y., Paxton, L. J., Wolven, B. C., Zhang, Y., Morrison, D., & Yeh, H. C. (2004). Coincident equatorial bubble detection by TIMED/GUVI and ROCSAT-1. *Geophysical Research Letters*, *31*, L03809. https://doi.org/10.1029/2003GL018696

Krall, J., Huba, J. D., Ossakow, S. L., Joyce, G., Makela, J. J., Miller, E. S., & Kelley, M. C. (2011). Modeling of equatorial plasma bubbles triggered by non-equatorial traveling ionospheric disturbances. *Geophysical Research Letters*, *38*, L08103. https://doi.org/10.1029/2011GL046890

Kudeki, E., Akgiray, A., Milla, M., Chau, J. L., & Hysell, D. L. (2007). Equatorial spread-F initiation: Post-sunset vortex, thermospheric winds, gravity waves. *Journal of Atmospheric and Solar-Terrestrial Physics*, *69*, 2416–2427. https://doi.org/10.1016/j.jastp.2007.04.012

Li, G., Ning, B., Abdu, M. A., Otsuka, Y., Yokoyama, T., Yamamoto, M., & Liu, L. (2013). Longitudinal characteristics of spread *F* backscatter plumes observed with the EAR and Sanya VHF radar in Southeast Asia. *Journal of Geophysical Research: Space Physics*, *118*, 6544–6557. https://doi.org/10.1002/jgra.50581

Li, G., Ning, B., Wang, C., Abdu, M. A., Otsuka, Y., Yamamoto, M., et al. (2018). Storm-enhanced development of post-sunset equatorial plasma bubbles around the meridian 120E/60W on 7-8 September 2017. *Journal of Geophysical Research: Space Physics*, *123*, 7985–7998. https://doi.org/10.1029/2018JA025871

Li, G., Otsuka, Y., Ning, B., Abdu, M. A., Yamamoto, M., Wan, W., et al. (2016). Enhanced ionospheric plasma bubble generation in more active ITCZ. *Geophysical Research Letters*, *43*, 2389–2395. https://doi.org/10.1002/2016GL068145

Lühr, H., Xiong, C., Park, J., & Rauberg, J. (2014). Systematic study of intermediate-scale structures of equatorial plasma irregularities in the ionosphere based on CHAMP observations. *Frontiers in Physics*, *2*, 15. https://doi.org/10.3389/fphy.2014.00015

Ma, G., & Maruyama, T. (2006). A super bubble detected by dense GPS network at east Asian longitudes. *Geophysical Research Letters*, *33*, L21103. https://doi.org/10.1029/2006GL027512

Makela, J. J. (2006). A review of imaging low-latitude ionospheric irregularity processes. *Journal of Atmospheric and Solar-Terrestrial Physics*, *68*, 1441–1458. https://doi.org/10.1016/j.jastp.2005.04.014

Mandal, S., Pallamraju, D., Karan, D. K., Phadke, K. A., Singh, R. P., & Suryawanshi, P. (2019). On deriving gravity wave characteristics in the daytime upper atmosphere using radio technique. *Journal of Geophysical Research: Space Physics*, *124*, 6985–6997. https://doi.org/10.1029/2019JA026723

Martinis, C., Baumgardner, J., Mendillo, M., Wroten, J., Coster, A., & Paxton, L. (2015). The night when the auroral and equatorial ionospheres converged. *Journal of Geophysical Research: Space Physics*, *120*, 8085–8095. https://doi.org/10.1002/2015JA021555

Martinis, C., Eccles, J. V., Baumgardner, J., Manzano, J., & Mendillo, M. (2003). Latitude dependence of zonal plasma drifts obtained from dual-site airglow observations. *Journal of Geophysical Research*, *108*(A3), 1129. https://doi.org/10.1029/2002JA009462

McClure, J. P., Singh, S., Bamgboye, D. K., Johnson, F. S., & Kil, H. (1998). Occurrence of equatorial *F* region irregularities: Evidence for tropospheric seeding. *Journal of Geophysical Research*, *103*, 29,119–29,136. https://doi.org/10.1029/98JA02749

Miller, E. S., Makela, J. J., & Kelley, M. C. (2009). Seeding of equatorial plasma depletions by polarization electric fields from middle latitudes: Experimental evidence. *Geophysical Research Letters*, *36*, L18105. https://doi.org/10.1029/2009GL039695

Nishioka, M., Saito, A., & Tsugawa, T. (2008). Occurrence characteristics of plasma bubble derived from global ground-based GPS receiver networks. *Journal of Geophysical Research*, *113*, A05301. https://doi.org/10.1029/2007JA012605

Otsuka, Y., Shiokawa, K., Ogawa, T., & Wilkinson, P. (2002). Geomagnetic conjugate observations of equatorial airglow depletions. *Geophysical Research Letters*, *29*(15), 1753. https://doi.org/10.1029/2002GL015347

Perkins, F. (1973). Spread *F* and ionospheric currents. *Journal of Geophysical Research*, *78*, 218–226. https://doi.org/10.1029/JA078i001p00218

Pimenta, A. A., Fagundes, P. R., Sahai, Y., Bittencourt, J. A., & Abalde, J. R. (2003). Equatorial *F*-region plasma depletion drifts: Latitudinal and seasonal variations. *Annales Geophysicae*, *21*, 2315–2322. https://doi.org/10.5194/angeo-21-2315-2003

Reinisch, B. W., & Huang, X. (2001). Deducing topside profiles and total electron content from bottomside ionograms. *Advances in Space Research*, *27*, 23–30. https://doi.org/10.1016/S0273-1177(00)00136-8

Retterer, J. M. (2010). Forecasting low-latitude radio scintillation with 3-D ionospheric plume models: 1. Plume model. *Journal of Geophysical Research*, *115*, A03306. https://doi.org/10.1029/2008JA013839

Retterer, J. M., & Roddy, P. (2014). Faith in a seed: On the origins of equatorial plasma bubbles. *Annales de Geophysique*, *32*, 485–498. https://doi.org/10.5194/angeo-32-485-2014

Rideout, W., & Coster, A. (2006). Automated gps processing for global total electron content data. *GPS Solutions*, *10*(3), 219–228. https://doi.org/10.1007/s10291-006-0029-5

Rishbeth, H. (1997). The ionospheric *E*-layer and *F*-layer dynamos—A tutorial review. *Journal of Atmospheric and Solar-Terrestrial Physics*, *59*, 1873–1880. https://doi.org/10.1016/S1364-6826(97)00005-9

Rodrigues, F. S., Hickey, D. A., Zhan, W., Martinis, C. R., Fejer, B. G., Milla, M. A., & Arratia, J. F. (2018). Multi-instrumented observations of the equatorial *F*-region during June solstice: Large-scale wave structures and spread- F. *Progress in Earth and Planetary Science*, *5*, 14. https://doi.org/10.1186/s40645-018-0170-0

Shiokawa, K., Otsuka, Y., Lynn, K. J., Wilkinson, P., & Tsugawa, T. (2015). Airglow-imaging observation of plasma bubble disappearance at geomagnetically conjugate points. *Earth, Planets and Space*, *67*, 43. https://doi.org/10.1186/s40623-015-0202-6

Smith, J., & Heelis, R. A. (2017). Equatorial plasma bubbles: Variations of occurrence and spatial scale in local time, longitude, season, and solar activity. *Journal of Geophysical Research: Space Physics*, *122*, 5743–5755. https://doi.org/10.1002/2017JA024128

Sun, L., Xu, J., Wang, W., Yuan, W., Li, Q., & Jiang, C. (2016). A statistical analysis of equatorial plasma bubble structures based on an all-sky airglow imager network in China. *Journal of Geophysical Research: Space Physics*, *121*, 11,495–11,517. https://doi.org/10.1002/2016JA022950

Takahashi, H., Wrasse, C. M., Otsuka, Y., Ivo, A., Gomes, V., Paulino, I., et al. (2015). Plasma bubble monitoring by TEC map and 630 nm airglow image. *Journal of Atmospheric and Solar-Terrestrial Physics*, *130*, 151–158. https://doi.org/10.1016/j.jastp.2015.06.003

Taori, A., Parihar, N., Ghodpage, R., Dashora, N., Sripathi, S., Kherani, E. A., & Patil, P. T. (2015). Probing the possible trigger mechanisms of an equatorial plasma bubble event based on multistation optical data. *Journal of Geophysical Research: Space Physics*, *120*, 8835–8847. https://doi.org/10.1002/2015JA021541

Tsunoda, R. T. (2010). On equatorial spread *F*: Establishing a seeding hypothesis. *Journal of Geophysical Research*, *115*, A12303. https://doi.org/10.1029/2010JA015564

Tsunoda, R. T. (2015). Upwelling: A unit of disturbance in equatorial spread F. *Progress in Earth and Planetary Science*, *2*, 9. https://doi.org/10.1186/s40645-015-0038-5

Tsunoda, R. T., Livingston, R. C., McClure, J. P., & Hanson, W. B. (1982). Equatorial plasma bubbles—Vertically elongated wedges from the bottomside F layer. *Journal of Geophysical Research*, *87*, 9171–9180. https://doi.org/10.1029/JA087iA11p09171

Tsunoda, R. T., Yamamoto, M., Tsugawa, T., Hoang, T. L., Tulasi Ram, S., Thampi, S. V., et al. (2011). On seeding, large-scale wave structure, equatorial spread *F*, and scintillations over Vietnam. *Geophysical Research Letters*, *38*, L20102. https://doi.org/10.1029/2011GL049173

Tulasi Ram, S., Ajith, K. K., Yokoyama, T., Yamamoto, M., & Niranjan, K. (2017). Vertical rise velocity of equatorial plasma bubbles estimated from Equatorial Atmosphere Radar (EAR) observations and HIRB model simulations. *Journal of Geophysical Research: Space Physics*, *122*, 6584–6594. https://doi.org/10.1002/2017JA024260

Tulasi Ram, S., Rama Rao, P. V. S., Prasad, D. S. V. V. D., Niranjan, K., Gopi Krishna, S., Sridharan, R., & Ravindran, S. (2008). Local time dependent response of postsunset ESF during geomagnetic storms. *Journal of Geophysical Research*, *113*, A07310. https://doi.org/10.1029/2007JA012922

Tulasi Ram, S., Yamamoto, M., Tsunoda, R. T., Chau, H. D., Hoang, T. L., Damtie, B., et al. (2014). Characteristics of large-scale wave structure observed from African and Southeast Asian longitudinal sectors. *Journal of Geophysical Research: Space Physics*, *119*, 2288–2297. https://doi.org/10.1002/2013JA019712

Vadas, S. L. (2007). Horizontal and vertical propagation and dissipation of gravity waves in the thermosphere from lower atmospheric and thermospheric sources. *Journal of Geophysical Research*, *112*, A06305. https://doi.org/10.1029/2006JA011845

Vadas, S. L., & Liu, H.-l. (2009). Generation of large-scale gravity waves and neutral winds in the thermosphere from the dissipation of convectively generated gravity waves. *Journal of Geophysical Research*, *114*, A10310. https://doi.org/10.1029/2009JA014108

Valladares, C. E., & Sheehan, R. (2016). Observations of conjugate MSTIDs using networks of GPS receivers in the American sector. *Radio Science*, *51*, 1470–1488. https://doi.org/10.1002/2016RS005967

Vierinen, J., Coster, A. J., Rideout, W. C., Erickson, P. J., & Norberg, J. (2016). Statistical framework for estimating GNSS bias. *Atmospheric Measurement Techniques*, *9*, 1303–1312. https://doi.org/10.5194/amt-9-1303-2016

Woodman, R. F., & La Hoz, C. (1976). Radar observations of *F* region equatorial irregularities. *Journal of Geophysical Research*, *81*(31), 5447–5466. https://doi.org/10.1029/JA081i031p05447

Xiong, C., Stolle, C., Lühr, H., Park, J., Fejer, B. G., & Kervalishvili, G. N. (2016). Scale analysis of equatorial plasma irregularities derived from Swarm constellation. *Earth, Planets and Space*, *68*, 121. https://doi.org/10.1186/s40623-016-0502-5

Yiğit, E., Medvedev, A. S., Aylward, A. D., Ridley, A. J., Harris, M. J., Moldwin, M. B., & Hartogh, P. (2012). Dynamical effects of internal gravity waves in the equinoctial thermosphere. *Journal of Atmospheric and Solar-Terrestrial Physics*, *90*, 104–116. https://doi.org/10.1016/j.jastp.2011.11.014

Yizengaw, E., & Groves, K. M. (2018). Longitudinal and seasonal variability of equatorial ionospheric irregularities and electrodynamics. *Space Weather*, *16*, 946–968. https://doi.org/10.1029/2018SW001980

Yokoyama, T., & Fukao, S. (2006). Upwelling backscatter plumes in growth phase of equatorial spread *F* observed with the Equatorial Atmosphere Radar. *Geophysical Research Letters*, *33*, L08104. https://doi.org/10.1029/2006GL025680

Zakharenkova, I., Astafyeva, E., & Cherniak, I. (2016). GPS and in situ Swarm observations of the equatorial plasma density irregularities in the topside ionosphere. *Earth, Planets and Space*, *68*, 120. https://doi.org/10.1186/s40623-016-0490-5

Zhang, S.-R., Erickson, P. J., Goncharenko, L. P., Coster, A. J., Rideout, W., & Vierinen, J. (2017). Ionospheric bow waves and perturbations induced by the 21 August 2017 solar eclipse. *Geophysical Research Letters*, *44*, 12,067–12,073. https://doi.org/10.1002/2017GL076054